

Prandtl number dependence of the small-scale properties in turbulent Rayleigh-Bénard convection

Shashwat Bhattacharya,^{1,*} Mahendra K. Verma,^{2,†} and Ravi Samtaney³

¹*Department of Mechanical Engineering,*

Indian Institute of Technology, Kanpur 208016, India

²*Department of Physics, Indian Institute of Technology, Kanpur 208016, India*

³*Mechanical Engineering, Division of Physical Science and Engineering, King Abdullah University of Science and Technology, Thuwal 23955, Saudi Arabia*

We analyze the Prandtl number (Pr) dependence of spectra and fluxes of kinetic energy, as well as the energy injection rates and dissipation rates, of turbulent thermal convection using numerical data. As expected, for a flow with $\text{Pr} \lesssim 1$, the inertial-range kinetic energy flux is constant, and the kinetic energy spectrum is Kolmogorov-like ($k^{-5/3}$). More importantly, we show that the amplitudes of the kinetic energy fluxes and spectra and those of structure functions increase with the decrease of Pr, thus exhibiting stronger nonlinearity for flows with small Prandtl numbers. Consistent with these observations, the kinetic energy injection rates and the dissipation rates too increase with the decrease of Pr. Our results are in agreement with earlier studies that report the Reynolds number to be a decreasing function of Prandtl number in turbulent convection. On the other hand, the tail of the probability distributions of the local heat flux grows with the increase of Pr, indicating increased fluctuations in the local heat flux with Pr.

I. INTRODUCTION

Turbulence is a complex phenomenon that remains largely unsolved even today. One of the important results of turbulence is due to Kolmogorov [1, 2] that explains the statistics of three dimensional (3D) turbulence under the assumption of homogeneity and isotropy. In Kolmogorov's model, the kinetic energy injected at large scales cascades down to intermediate scales, called the inertial range, and then to dissipative scales. Kolmogorov's theory assumes that in the inertial range, no kinetic energy is injected and the viscous dissipation rate is negligible. This leads to the energy cascade rate Π_u , also referred to as the kinetic energy flux, being constant in the inertial range and equal to the total viscous dissipation rate ϵ_u . Dimensional analysis leads to the following relation for the energy spectrum $E_u(k)$:

$$E_u(k) = K_{\text{KO}}(\epsilon_u)^{2/3} k^{-5/3}, \quad (1)$$

* shabhatt@iitk.ac.in

† mkv@iitk.ac.in

where k is the wavenumber, and K_{KO} is the Kolmogorov constant [3, 4].

The dynamics become more involved in turbulent thermal convection. In such flows, buoyancy acts at all scales, including the inertial range, and thus can potentially alter the scaling of kinetic energy spectrum and flux, as discussed by Bolgiano [5], Obukhov [6], Procaccia and Zeitak [7], L’vov [8], L’vov and Falkovich [9], and Kumar *et al.* [10]. Also, refer to reviews Ahlers *et al.* [11], Lohse and Xia [12], Chillà and Schumacher [13], and Verma [14, 15] for further details. A large number of such works focus on an idealized setup called Rayleigh-Bénard convection (RBC) where a fluid is enclosed between two horizontal walls with the bottom wall kept at a higher temperature than the top wall [16]. RBC is governed by two dimensionless parameters: the Rayleigh number (Ra), which is the ratio of the buoyancy and the dissipative forces, and the Prandtl number (Pr), which is the ratio of kinematic viscosity to thermal diffusivity.

For stably-stratified turbulence, Bolgiano [5] and Obukhov [6] proposed that the energy and entropy spectra scale as $E_u(k) \sim k^{-11/5}$ and $E_\theta(k) \sim k^{-7/5}$ respectively for $k < k_B$, the Bolgiano wavenumber, where buoyancy forces are strong. The aforementioned scaling will be henceforth referred to as Bolgiano-Obukhov (BO) scaling. For $k > k_B$, the buoyancy forces are weak and Kolmogorov-Obukhov scalings of $E_u(k) \sim k^{-5/3}$ and $E_\theta(k) \sim k^{-5/3}$ are expected. Using theoretical arguments, Procaccia and Zeitak [7], L’vov [8], L’vov and Falkovich [9], and Rubinstein [17] proposed the applicability of BO scaling to RBC as well. Researchers have attempted to confirm the above theory with the help of experiments and numerical simulations. Many researchers have reported BO scaling in RBC [18–24] based on their observations, except for convection in the small Pr regime, where Kolmogorov-Obukhov scaling was reported [25–31]. In a critical review, Lohse and Xia [12] raised doubts on BO phenomenology in RBC.

Recent works on turbulent RBC show that thermal plumes inject kinetic energy to the system, hence the kinetic energy flux is a non-decreasing function of k , thus ruling out BO scaling for turbulent thermal convection [10, 32]. They also observed that in the inertial range of Pr = 1 RBC, the kinetic energy injection rates by buoyancy is relatively weak, hence the kinetic energy flux is nearly constant, and the energy spectrum is Kolmogorov-like ($k^{-5/3}$). Some other works [30, 31, 33–35] too reported similar behaviour. Note however that large-Pr convection exhibits much steeper kinetic energy spectrum due to strong viscous dissipation [36, 37].

In this paper, we perform detailed numerical simulations of RBC for a fixed Ra = 10^7 and Pr = 0.02, 0.1, 1, 6.8, and 100, and analyze the relative magnitudes of energy fluxes and spectra. We observe that turbulence gets stronger with the decrease of Prandtl number. Interestingly, the magnitudes of entropy (θ^2 , where θ is the temperature fluctuation from the conduction profile) spectra and fluxes do not change significantly with the Prandtl number. Even though we focus on a small set of parameters, the patterns observed here are expected to be valid for a wide range of parameters. Note, however, that there might be a different pattern in the ultimate regime of very large Rayleigh numbers [38] on which intense research

is still going on.

The structure function is directly related to the energy spectrum [15, 39]. For homogeneous and isotropic 3D turbulence, the third-order velocity structure function scales as $S_3^u(l) \sim -l$, where l is the length scale [1, 2]. The higher order structure functions for such flows fit well with the hierarchy model of She and Leveque [40]. Although there have been many studies on structure functions of thermal convection for moderate Prandtl numbers [12, 33, 41–49], their reported scalings are not very conclusive. Recently, using high resolution numerical simulations of convection for $Pr = 1$, Bhattacharya *et al.* [50] showed that the structure functions of thermal convection scale similarly as that of 3D hydrodynamic turbulence. Note that these works are for $Pr \leq 7$. In this paper, we analyze the structure functions for Pr ranging from 0.02 to 100 and show that their amplitudes increase with the decrease of Prandtl number, similar to the amplitudes of the energy spectra.

In turbulent convection, buoyancy injects kinetic energy at all scales, including the dissipation range. Bhattacharya *et al.* [50] showed that for $Pr = 1$ convection, although the modal kinetic energy injection by buoyancy is small at intermediate wavenumbers (as discussed earlier), it adds up to a significant fraction of the total kinetic energy injection when summed over the inertial and dissipative scales. The inertial-range kinetic energy flux is due to the fraction of energy injected only at large scales and hence less than the total kinetic-energy dissipation rate. We expect the kinetic-energy dissipation rate and the energy injection rates by buoyancy to exhibit a similar Pr dependence as the energy flux. Our numerical simulations are consistent with these arguments.

Even though heat flows from the bottom plate to top plate, there are strong fluctuations in the local heat flux [33, 51–53]. These above works reveal both negative and positive local heat fluxes with exponential tails in RBC. However, the positive heat fluxes dominate the negative ones, leading to a net vertical heat flux. Similar asymmetry has been observed in many other systems, for example in wave turbulence [54]. In this paper, we report the Prandtl number dependence of the probability distribution of the convective heat flux.

In RBC, the global heat transport and the large-scale velocity are quantified by the Nusselt number (Nu) and the Reynolds number (Re) respectively [55–57]. Many experiments and simulations of RBC have been performed to study the variations of these quantities with Pr . These studies revealed that Nu is a very weak function of Pr for $Pr \gtrsim 1$ [58–61] but varies as $Nu \sim Pr^{0.14}$ for $Pr \ll 1$ [58]. Further, the scaling of Re has been shown to vary from $Re \sim Pr^{-0.7}$ for $Pr \ll 1$ to $Re \sim Pr^{-1}$ for $Pr \gg 1$ [58, 60, 62]. These observations have been explained by several models [55, 56, 63, 64]. In this paper, we will not discuss the scaling of large-scale quantities. However, it must be noted that our current observations on the variations of the amplitudes of the spectral quantities and the velocity structure functions with Prandtl number are consistent with the aforementioned studies [58, 60, 62] that report Re to be a decreasing function of Pr .

The outline of the paper is as follows. In Sec. II, we present the governing equations of RBC and briefly introduce the spectral quantities that will be analyzed in this work. We

discuss the simulation details in Sec. III. In Sec. IV, we obtain the Pr dependence on the spectral quantities using our simulation data. In Sec. V, we discuss the scaling of velocity structure functions for different Pr. In Sec. VI, we study the probability distribution of the convective heat flux. We conclude in Sec. VII. The entropy spectra and fluxes for various Prandtl numbers are discussed in Appendix A.

II. REVIEW OF ENERGY SPECTRUM, ENERGY FLUX, AND STRUCTURE FUNCTIONS OF RBC

The governing equations of RBC under the Boussinesq approximation [16] are as follows:

$$\frac{\partial \mathbf{u}}{\partial t} + (\mathbf{u} \cdot \nabla) \mathbf{u} = -\frac{\nabla \sigma}{\rho_0} + \alpha g \theta \hat{z} + \nu \nabla^2 \mathbf{u}, \quad (2)$$

$$\frac{\partial \theta}{\partial t} + (\mathbf{u} \cdot \nabla) \theta = \frac{\Delta}{d} u_z + \kappa \nabla^2 \theta, \quad (3)$$

$$\nabla \cdot \mathbf{u} = 0, \quad (4)$$

where \mathbf{u} and σ are the velocity and the pressure fields respectively, θ is the fluctuation of temperature from conduction state, and Δ and d are the temperature difference and distance respectively between the top and bottom walls.

We nondimensionalize Eqs. (2) to (4) using d as the length scale, $\sqrt{\alpha g \Delta d}$ as the velocity scale, and Δ as the temperature scale. The nondimensionalized variables are as follows [58, 65].

$$\mathbf{u}' = \frac{\mathbf{u}}{\sqrt{\alpha g \Delta d}}, \quad \nabla' = \nabla d, \quad \theta' = \frac{\theta}{\Delta}, \quad t' = \frac{\sqrt{\alpha g \Delta d}}{d} t, \quad \sigma' = \frac{\sigma}{\rho_0 \alpha g \Delta d}. \quad (5)$$

The governing equations in terms of the nondimensional variables become

$$\frac{\partial \mathbf{u}'}{\partial t'} + \mathbf{u}' \cdot \nabla' \mathbf{u}' = -\nabla' \sigma' + \theta' \hat{z} + \sqrt{\frac{\text{Pr}}{\text{Ra}}} \nabla'^2 \mathbf{u}', \quad (6)$$

$$\frac{\partial \theta'}{\partial t'} + \mathbf{u}' \cdot \nabla' \theta' = u'_z + \frac{1}{\sqrt{\text{RaPr}}} \nabla'^2 \theta', \quad (7)$$

$$\nabla' \cdot \mathbf{u}' = 0, \quad (8)$$

where $\text{Ra} = \alpha g \Delta d^3 / (\nu \kappa)$ is the Rayleigh number, and $\text{Pr} = \nu / \kappa$ is the Prandtl number. The Rayleigh and Prandtl numbers are the governing parameters of RBC. The primes for the nondimensional variables will henceforth be dropped for the sake of brevity.

We now describe the important quantities that will be used for analyzing the statistics of RBC in this paper. These are the kinetic energy spectrum, kinetic energy flux, buoyant energy injection spectrum, viscous dissipation spectrum, and the velocity structure functions. The kinetic energy spectrum [3, 4] is the kinetic energy contained in a wavenumber shell of radius k . It is defined as

$$E_u(k) = \frac{1}{2} \sum_{k \leq |\mathbf{k}'| < k+1} |\mathbf{u}(\mathbf{k}')|^2, \quad (9)$$

where $\mathbf{u}(\mathbf{k})$ is the Fourier transform of the velocity field. The kinetic energy is injected by buoyancy predominantly at large scales, but some energy is also injected at small scales [12, 14, 15, 32, 66]. The energy injection spectrum $\mathcal{F}_B(k)$ in its nondimensional form is given by [3, 4]

$$\mathcal{F}_B(k) = \sum_{|\mathbf{k}|=k} \Re\{\mathbf{u}(\mathbf{k}) \cdot \mathbf{f}^*(\mathbf{k})\} = \sum_{|\mathbf{k}|=k} \Re\{u_z(\mathbf{k})\theta^*(\mathbf{k})\}. \quad (10)$$

where $\mathbf{f} = \theta\hat{z}$ is the buoyancy term in the nondimensional momentum equation and $*$ represents the complex conjugate. The injected kinetic energy cascades to smaller scales by nonlinear interactions between different velocity modes. This transfer of energy is quantified by energy flux Π_u , which is the kinetic energy leaving a wavenumber sphere of radius k_0 . The flux is computed as follows [67–69]:

$$\Pi_u(k_0) = \sum_{k \geq k_0} \sum_{p < k_0} \delta_{\mathbf{k}, \mathbf{p}+\mathbf{q}} \Im([\mathbf{k} \cdot \mathbf{u}(\mathbf{q})][\mathbf{u}^*(\mathbf{k}) \cdot \mathbf{u}(\mathbf{p})]). \quad (11)$$

The kinetic energy gets dissipated predominantly at small scales due to viscosity. This phenomenon is quantified by the viscous dissipation spectrum, which in nondimensional form is given by [3, 4]

$$D(k) = 2\sqrt{\frac{\text{Pr}}{\text{Ra}}} k^2 E_u(k), \quad (12)$$

with the total viscous dissipation rate being $\epsilon_u = \sum_0^\infty D(k)$. In real space, the total viscous dissipation rate is also given by

$$\epsilon_u = 2\sqrt{\text{Pr}/\text{Ra}} \langle S_{ij} S_{ij} \rangle, \quad (13)$$

where S_{ij} is the strain rate tensor [70]. The aforementioned spectral quantities are related to each other by the variable energy flux equation [3, 4, 15], which for a steady state is

$$\frac{d}{dk} \Pi_u(k) = \mathcal{F}_B(k) - D(k). \quad (14)$$

Note that for a steady state, the total kinetic energy injection rate $\sum_0^\infty \mathcal{F}_B(k)$ equals the total viscous dissipation rate ϵ_u [3, 4].

Apart from the energy spectrum, the structure function is another important diagnostics tool to describe turbulence. The velocity structure function of order q is defined as [3, 4, 39]

$$S_q^u(l) = \langle [(\mathbf{u}(\mathbf{r} + \mathbf{l}) - \mathbf{u}(\mathbf{r})) \cdot \hat{\mathbf{l}}]^q \rangle, \quad (15)$$

where \mathbf{r} and \mathbf{l} are position vectors, and $l = |\mathbf{l}|$. The second-order velocity structure function is related to the energy spectrum [4, 39].

In this paper, we compute and compare the above quantities for different Prandtl numbers using data from numerical simulations. In the next section, we discuss the numerical methods employed in our study.

TABLE I. Details of our data obtained from direct numerical simulations of RBC performed in a cubical box for $Ra = 10^7$: the Prandtl number (Pr), the grid size, the ratio of the Kolmogorov length scale (for $Pr \leq 1$) or the Batchelor length scale (for $Pr > 1$) to the mesh width ($\eta/\Delta x$), the number of grid points in viscous and thermal boundary layers (N_{VBL} and N_{TBL} respectively), the Nusselt number (Nu), the number of non-dimensional time units (t_{ND}), and snapshots over which the quantities are averaged.

Pr	Grid size	$\eta/\Delta x$	N_{VBL}	N_{TBL}	Nu	t_{ND}	Snapshots
0.02	1025^3	1.45	7	48	10.6 ± 0.6	8	81
0.1	513^3	1.52	6	20	13.9 ± 1.1	33	66
1	257^3	2.31	5	9	16.3 ± 1.3	101	101
6.8	257^3	2.33	6	9	15.9 ± 1.2	101	101
100	257^3	2.30	7	9	16.8 ± 1.3	101	101

III. DETAILS OF OUR NUMERICAL SIMULATIONS

We numerically solve Eqs. (6)-(8) for Pr from 0.02 to 100 for a fixed Rayleigh number of $Ra = 10^7$ to study Pr dependence of turbulent thermal convection. The simulations were performed on a cubical domain of unit dimension using the finite difference solver SARAS [71, 72]. The solver uses a second-order spatial discretization scheme and employs multigrid method for solving the pressure-Poisson equations. No-slip boundary conditions were imposed on all the walls, adiabatic boundary conditions on the sidewalls and isothermal boundary conditions on the top and bottom walls. A second-order Crank-Nicholson scheme was used for time-advancement, and the maximum Courant number was kept at 0.7. The maximum time for simulations range from 3 to 101 free-fall time (t_{ND}) after attaining a steady state.

The grid resolutions were varied from 257^3 for $Pr = 100$ to 1025^3 for $Pr = 0.02$. The above grid resolutions ensure that the grid-spacing Δx is smaller than the Kolmogorov length scale $\eta = (\nu^3 \epsilon_u^{-1})^{1/4}$ for $Pr \leq 1$ and the Batchelor length scale $\eta_\theta = (\nu \kappa^2 \epsilon_u^{-1})^{1/4}$ for $Pr > 1$, indicating that the smallest scales of the simulations are adequately resolved. Further, we have a minimum of 7 points in the viscous and thermal boundary layers, satisfying the resolution criterion of Grötzbach [73] and Verzicco and Camussi [74]. We validate our simulations by computing the Nusselt number (see Sec. VI) for all our runs and ensuring that they are consistent with earlier results [57, 75–79]. We also compute the Nusselt number averaged over the last half of the free-fall time range for every run and observe it to match with the Nusselt number averaged over the entire free-fall time range, with the deviation being within approximately 2%. Thus, we verify that our simulations are statistically converged. The simulation details are summarized in Table I.

We employ the pseudo-spectral code TARANG [80, 81] to compute the spectra and fluxes

of kinetic energy. To compute the Fourier transform of velocity fields, we approximate the velocity field using free-slip boundary conditions [14], and employ Fourier (sine and cosine) expansion of the field. Note that the viscous boundary layer thickness is very small (less than 5% of the domain size [82]), and the small-scale structures in the boundary layers do not affect the inertial-range properties [14, 15]. Hence, even for flows bounded by rigid walls, the inertial-range spectra and fluxes can be computed using Fourier expansion with reasonable accuracy. Since the boundary layers are thin, the system can be considered homogeneous. The Fourier expansion of the velocity field is as follows [14].

$$u_x(x, y, z) = \sum_{k_x, k_y, k_z} u_x(k_x, k_y, k_z) 8 \sin(k_x x) \cos(k_y y) \cos(k_z z), \quad (16)$$

$$u_y(x, y, z) = \sum_{k_x, k_y, k_z} u_y(k_x, k_y, k_z) 8 \cos(k_x x) \sin(k_y y) \cos(k_z z), \quad (17)$$

$$u_z(x, y, z) = \sum_{k_x, k_y, k_z} u_z(k_x, k_y, k_z) 8 \cos(k_x x) \cos(k_y y) \sin(k_z z), \quad (18)$$

where $k_x = l\pi$, $k_y = m\pi$, and $k_z = n\pi$; l , m , and n are positive integers. Using the values of $u_x(k_x, k_y, k_z)$, $u_y(k_x, k_y, k_z)$, and $u_z(k_x, k_y, k_z)$, we compute the kinetic energy spectrum and flux using Eqs. (9) and (11) respectively. The total kinetic energy injection and dissipation rates are computed using Eq. (13).

In RBC, since buoyancy is only along the vertical direction, the flow is expected to be anisotropic. Interestingly, however, Nath *et al.* [83] showed via detailed numerical simulations that RBC is nearly isotropic. In the aforementioned work, Nath *et al.* [83] computed the modal kinetic energy as a function of the polar angle Θ (angle between the buoyancy direction and the wavenumber) and found it to be nearly independent of Θ . Based on the results of the above work, the minor directional dependence of the modal kinetic energy can be neglected, and we analyze the spectral quantities as functions of the wavenumber shell radius (k) in this paper.

We use the parallel code `fastSF` [84] to compute the velocity structure functions. Since RBC is nearly homogeneous and isotropic as described earlier, we average the structure functions over the entire domain. For our computations, we coarse-grain our data to a 256^3 grid in order to save computational resources. Note that the aforementioned coarse-graining filters the dissipation scale and it does not impact the inertial range scaling. All the spectral quantities and structure functions are averaged over 30 to 100 snapshots taken at equal time intervals after attaining a steady state.

In the next three sections, we present our numerical results.

IV. VARIATION OF SPECTRAL QUANTITIES WITH PRANDTL NUMBER

In this section, we analyse the Pr dependence of the kinetic energy spectra, kinetic energy fluxes, energy injection rates, and dissipation rates using our numerical data.

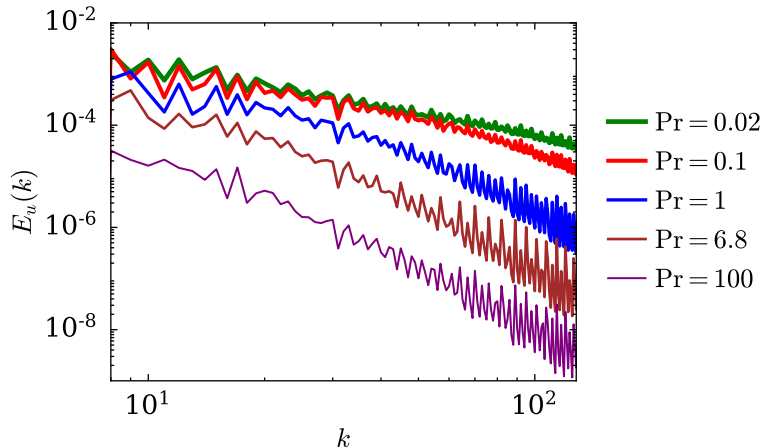


FIG. 1. (color online) (a) For $Ra = 10^7$ and $Pr = 0.02$ (green), 0.1 (red), 1 (black), 6.8 (brown), and 100 (purple): plots of the kinetic energy spectra versus the wavenumber k . The spectra exhibits fluctuations at small and intermediate wavenumbers.

A. Kinetic energy spectra and fluxes

We compute the kinetic energy spectrum ($E_u(k)$) and flux ($\Pi_u(k)$) for all our runs using Eqs. (9,11). In Fig. 1 exhibits the plots of the kinetic energy spectra for different Prandtl numbers. We note that energy spectrum exhibits fluctuations at small and intermediate wavenumbers that produce large errors in the best-fit curves [85]. To mitigate these errors, we employ best-fit curves for the *integral energy spectrum*, which is $\int_k^\infty E_u(k')dk' = \sum_k^\infty E_u(k')$. The integration process smoothens the curves significantly leading to a major reduction in fitting errors.

For the inertial-range spectral form of $E_u(k) \sim k^\alpha$, the integral $\sum_k^\infty E_u(k') \sim k^{\alpha+1}$, thus, the fit functions to the integral energy spectrum provides us the spectral index α . We plot $\sum_k^\infty E_u(k')$ and $\Pi_u(k)$ versus k in Fig. 2(a,b). The figure shows that For $Pr \leq 1$, $\sum_k^\infty E_u(k')$ scales as $k^{-2/3}$ for intermediate wavenumbers, which translates to Kolmogorov's energy spectrum ($E_u(k) \sim k^{-5/3}$). The errors in the exponents obtained from the best fits range from ± 0.01 to ± 0.07 . Further, consistent with the observed Kolmogorov's energy spectrum, $\Pi_u(k)$ is approximately constant over these wavenumbers. Our results, which are based on convection with no-slip walls, are consistent with earlier works [10, 31, 32, 66] on small and moderate Pr convection but with free-slip walls. These observations rule out Bolgiano-Obukhov scaling ($E_u(k) \sim k^{-11/5}$) for thermal convection. Earlier, based on positive kinetic-energy injection rate by buoyancy, Kumar *et al.* [10] and Verma *et al.* [32] had argued in favour of Kolmogorov's spectrum for turbulent convection.

For $Pr = 6.8$ and 100 , the kinetic energy flux $\Pi_u(k)$ decreases sharply with k in the inertial range. Thus, instead of Kolmogorov's spectrum, we obtain a much steeper energy

spectrum: $\sum_k^\infty E_u(k') \sim k^{-2.49}$ for $\text{Pr} = 6.8$ and $\sim k^{-2.62}$ for $\text{Pr} = 100$, with an error of ± 0.01 in the exponents. These relations translate to $E_u(k) \sim k^{-3.49}$ for $\text{Pr} = 6.8$ and $\sim k^{-3.62}$ for $\text{Pr} = 100$. For $\text{Pr} \rightarrow \infty$, Pandey *et al.* [36] derived that $E_u(k) \sim k^{-13/3}$. Note that the energy spectra for $\text{Pr} = 6.8$ and 100 are quite close to the energy spectrum for $\text{Pr} \rightarrow \infty$, consistent with the earlier results on energy spectra and fluxes [14, 36, 37].

Now, we explore the Pr dependence of the amplitudes of the kinetic energy spectra and fluxes. Figure 2(a,b) shows that for the same Ra , convection with small Pr has more kinetic energy than that with large Pr . This is because the nonlinear interactions among the velocity modes for small- Pr convection are stronger than those for large- Pr convection. Our results are in agreement with the earlier studies that report the Reynolds number (which indicates the strength of nonlinearities) to be a decreasing function of Pr [11, 58, 60, 62]. Further, for $\text{Pr} \leq 1$, the width of the wavenumbers' range over which Kolmogorov's scaling is observed decreases with the increase of Pr : $8 \leq k \leq 60$ for $\text{Pr} = 0.02$ and $6 \leq k \leq 17$ for $\text{Pr} = 1$. Note, however, that for large Prandtl numbers, power law regimes are observed at much larger wavenumbers.

Having analyzed the energy spectra and fluxes, we now examine the variations of the

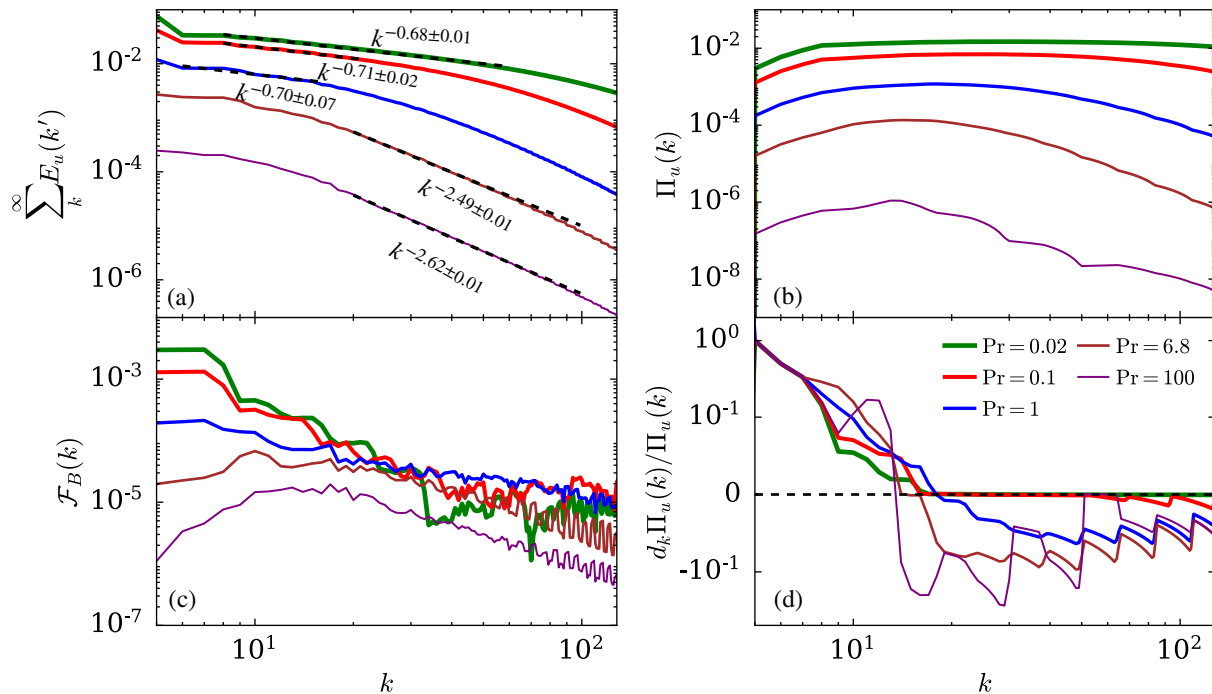


FIG. 2. (color online) For $\text{Ra} = 10^7$ and $\text{Pr} = 0.02, 0.1, 1, 6.8, \text{ and } 100$: (a) Integral kinetic energy spectrum, $\sum_k^\infty E_u(k')$ vs. wavenumber k , (b) kinetic energy flux, $\Pi_u(k)$, vs. k , (c) energy injection rate due to buoyancy, $\mathcal{F}_B(k)$, vs. k , and (d) $d_k \Pi_u(k) / \Pi_u(k)$ vs. k . The amplitudes of the energy spectrum and flux decrease with Pr . For $\text{Pr} \leq 1$, the energy spectrum exhibits Kolmogorov's scaling.

kinetic energy injection rates $\mathcal{F}_B(k)$ with Pr. We plot $\mathcal{F}_B(k)$ versus k for different Prandtl numbers in Fig. 2(c). These plots reveal that $\mathcal{F}_B(k)$ is positive for all Pr, implying that buoyancy feeds kinetic energy to the system. This observation is in agreement with the findings of Kumar *et al.* [10] and Verma *et al.* [32] for Pr = 1 and contradicts the earlier arguments favoring BO scaling in RBC [7–9, 17, 19, 20, 41–44, 47].

Figure 2(c) also shows that the kinetic energy injection is the strongest for Pr = 0.02 and becomes weaker as Pr increases, similar to the energy spectrum and flux. Further, for small Prandtl numbers, $\mathcal{F}_B(k)$ drops sharply with k compared to larger Prandtl numbers. This is because, in the limit of Pr \rightarrow 0, $\mathcal{F}_B(k)$ scales as $\text{Ra}\langle|u_z(k)|^2\rangle/k^2$ [14, 31], which shows that $\mathcal{F}_B(k)$ decreases steeply with k . Thus, for small and moderate Prandtl numbers, $\mathcal{F}_B(k)$ is small in the inertial range compared to the energy flux and cannot bring significant variations in $\Pi_u(k)$ in that regime. This results in Kolmogorov-like scaling of the kinetic energy spectrum for small and moderate-Pr convection, consistent with the arguments of earlier studies [10, 31, 32, 86].

In Fig. 2(d), we plot the normalized derivative of the kinetic energy flux, $d_k\Pi_u/\Pi_u(k)$, versus k for different Pr (d_k denotes the derivative with respect to k). Recall from Eq. (14) that $d_k\Pi_u(k) = \mathcal{F}_B(k) - D(k)$. Since energy is dissipated at small scales, $D(k)$ becomes stronger than $\mathcal{F}_B(k)$ at large wavenumbers, causing the kinetic energy flux to be a decreasing function of k . As evident in Fig. 2(d), the crossover wavenumber at which the derivative of the flux changes sign decreases with increasing Pr: $k = 33$ for Pr = 0.02 and $k = 14$ for Pr = 100. This is expected; since Ra is constant in all the runs, the flow is more viscous and less thermally diffusive by the same factor for increasing Pr. Hence, $D(k)$ is strong even at intermediate scales [36]. For Pr = 6.8 and 100, $D(k)$ exceeds $\mathcal{F}_B(k)$ by a significant amount at intermediate scales, resulting in $d_k\Pi_u(k)/\Pi_u(k) \lesssim -0.1$. Thus, $\Pi_u(k)$ decreases sharply with k for these Prandtl numbers in the intermediate scales, leading to a steeper energy spectrum compared to $k^{-5/3}$, consistent with the findings of Pandey *et al.* [36, 37].

These results provide a comprehensive picture for the variations of kinetic energy spectra and fluxes of thermal convection with Pr. In the next subsection, we discuss how the strength of the nonlinear interactions in RBC vary with Pr.

B. Energy flux and viscous dissipation in thermal convection

In 3D hydrodynamic turbulence, the kinetic energy flux in the inertial range matches with the total dissipation rate. This is not the case in turbulent thermal convection because buoyancy feeds energy at all scales, including the dissipation range. Consequently, $\Pi_u < \epsilon_u$. Bhattacharya *et al.* [50] showed that for Pr = 1, the inertial-range kinetic energy flux is approximately one-third of the total dissipation rate. In this subsection, we will describe these quantities for various Prandtl numbers.

In Fig. 3, we plot the total viscous dissipation rate (ϵ_u) along with the maximum inertial

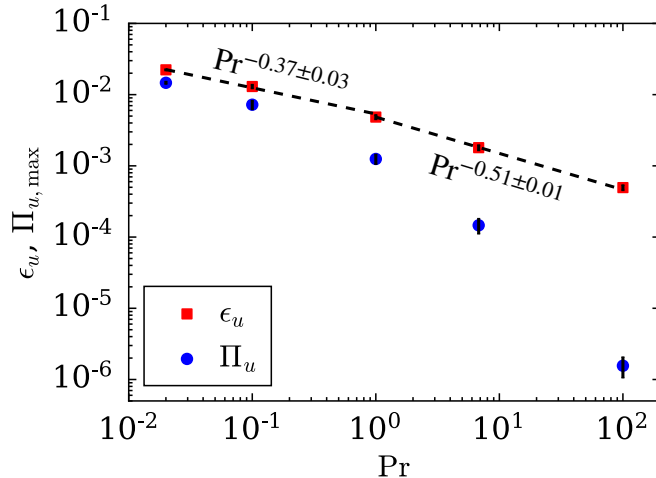


FIG. 3. (color online) For $Ra = 10^7$: Plots of ϵ_u and maximum kinetic energy flux $\Pi_{u,\max}$ vs. k . The dissipation rates decrease with the increase of Pr , similar to the energy spectrum and flux. The difference between the kinetic energy flux and the dissipation rate increases as Pr is increased.

range kinetic energy flux ($\Pi_{u,\max}$) versus Pr . The figure shows that ϵ_u decreases with the increase of Pr as $Pr^{-0.37}$ for $Pr < 1$, and as $Pr^{-0.51}$ for $Pr \geq 1$. Our observations are consistent with the fact that the nonlinear interactions among the velocity modes decrease with increasing Pr . It is also clear from Fig. 3 that $\Pi_{u,\max} < \epsilon_u$ as discussed earlier. Further, the difference between $\Pi_{u,\max}$ and ϵ_u increases as Pr is increased. Recall from Sec. IV A that the kinetic energy injection rate $\mathcal{F}_B(k)$ decreases steeply with k for small Pr and becomes progressively less steep as Pr is increased [as exhibited in Fig. 2(c)]. This indicates that for small Pr , most of the energy is injected at large scales, as a result of which the inertial range kinetic energy flux is only marginally less than the total dissipation rate. Thus, small Pr convection is close to 3D hydrodynamic turbulence where $\Pi_u \approx \epsilon_u$. On the other hand, for large Pr , only a small fraction of the total energy is injected at large scales and a significant amount of kinetic energy is injected in the inertial and dissipation ranges. Therefore, the inertial-range flux is much less than ϵ_u . For $Pr = 100$, the inertial-range kinetic energy flux is about three orders of magnitude smaller than the dissipation rate.

Now, we compare the scaling of ϵ_u in RBC and hydrodynamic turbulence. For the latter,

$$\epsilon_u \approx U^3/d,$$

where U is the large scale velocity (for example, the root mean square velocity), and d is the size of the domain. However, in thermal convection, Pandey and Verma [57] and Pandey *et al.* [75] showed that for $Pr = 1$,

$$\epsilon_u \sim (U^3/d)Ra^{-0.18},$$

instead of U^3/d ; here U is the root mean square velocity. The additional Ra dependence was attributed to multiscale forcing by buoyancy and to the suppression of nonlinear interactions

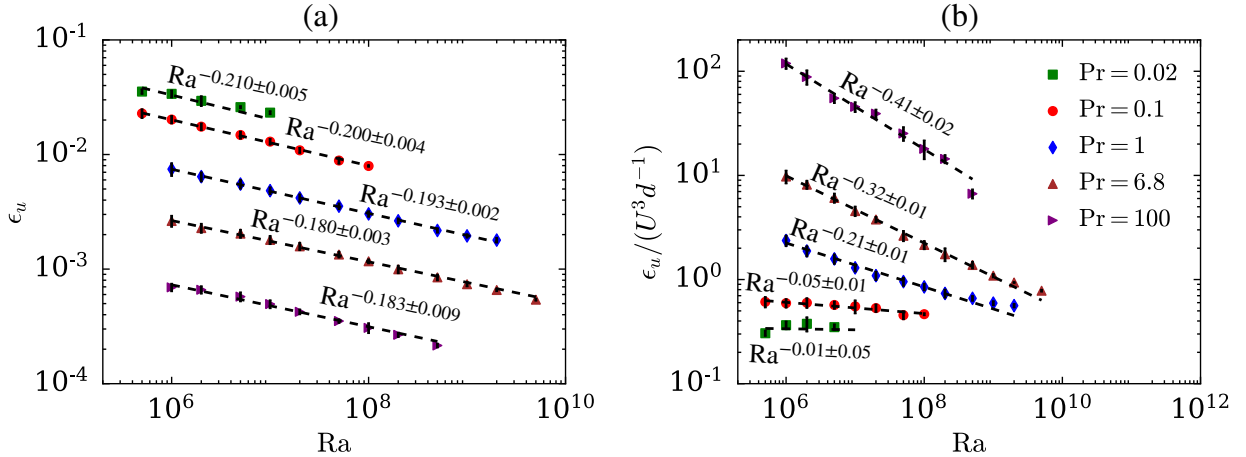


FIG. 4. (color online) For $Pr = 0.02, 0.1, 1, 6.8$, and 100 , (a) plots of ϵ_u vs. Ra , and (b) plots of $\epsilon_u/(U^3/d)$ vs. Ra (data taken from Bhattacharya *et al.* [82]). For small Pr , $\epsilon_u \sim U^3/d$ as in hydrodynamic turbulence. However, ϵ_u has an additional Ra dependence for larger Prandtl numbers.

due to the presence of walls. Motivated by these observations, we investigate the scaling of viscous dissipation rate for various Prandtl numbers. Towards this objective, we use additional datasets of Bhattacharya *et al.* [82] that include simulations for Ra ranging from 5×10^5 to 2×10^9 and Pr ranging from 0.02 to 100 . In Fig. 4(a), we plot ϵ_u versus Ra . We compute $\epsilon_u/(U^3/d)$ for all the data points and plot them versus Ra in Fig. 4(b). We also plot the best-fit curves for our data on the above figures.

Figure 4(a) shows that the viscous dissipation rate ϵ_u decreases with Ra as $Ra^{-\alpha}$, where α ranges from 0.21 for $Pr = 0.02$ to 0.18 for $Pr = 6.8$ and 100 . Our results are consistent with those of Scheel and Schumacher [78], who also observed a similar value for the exponent α and its variations with Pr . Figure 4(b) shows that for $Pr = 0.02$, $\epsilon_u \sim U^3/d$, similar to hydrodynamic turbulence. However, for larger Pr , $\epsilon_u/(U^3/d)$ decreases with Ra with slopes getting steeper with the increase of Pr . For $Pr = 100$, ϵ_u has a strong Ra correction with $\epsilon_u \sim (U^3/d)Ra^{-0.41}$. The strong Ra dependence for large Pr is due to strong viscous dissipation in such flows.

In the next section, we discuss the Pr dependence on the velocity structure functions of turbulent convection.

V. STRUCTURE FUNCTIONS

In this section, we examine the velocity structure functions of turbulent convection using our numerical data.

For homogeneous and isotropic 3D hydrodynamic turbulence, Kolmogorov [1, 2] proved

the following exact relation for the third-order structure function:

$$S_3^u(l) = -\frac{4}{5}\epsilon_u l \sim -l. \quad (19)$$

However, for $q \neq 3$, the velocity structure functions scale as $S_q^u(l) \sim \pm l^{\zeta_q}$, where ζ_q is the exponents for q -th order structure function. Note that a simple extrapolation of Kolmogorov's theory to higher-order structure functions yields $\zeta_q = q/3$ (labelled as KO41 model). Several experimental and numerical results however do not agree with this prediction. Among many models, such as β model, multifractal model, log-normal model [3, 87, 88], the model by She and Leveque [40] provides the best fit function to ζ_q , which is

$$\zeta_q = \frac{q}{9} + 2 \left(1 - \left(\frac{2}{3} \right)^{q/3} \right). \quad (20)$$

This model is labelled as SL94. The differences between the KO41 and SL94 are attributed to the *intermittency effects* [3, 87].

For turbulent thermal convection, some researchers have argued in favour of KO41 model, while some others have argued that $\zeta_q = 3q/5$, which is derived from Bolgiano-Obukhov scaling (labelled as BO59). For example, Benzi *et al.* [41, 42] computed the structure functions upto sixth order using numerical data and reported BO59 scaling of $S_q^u(l) \sim l^{3q/5}$. Ching [43], Calzavarini *et al.* [44], and Kunnen *et al.* [47] also observed BO59 scaling. On the other hand, Sun *et al.* [46], and Kaczorowski and Xia [33] reported KO41 scaling for the lower order structure functions of RBC. Recently, Bhattacharya *et al.* [50] showed that the third-order velocity structure function of RBC for $\text{Pr} = 1$ obeys Eq. (19), similar to hydrodynamic turbulence, except that ϵ_u is replaced with Π_u . Sun *et al.* [46] and Bhattacharya *et al.* [50] showed that the exponents for the higher order structure functions of convection follow She-Leveque's model given by Eq. (20).

Note that the above works are for a specific set of parameters, and they do not provide us with a comprehensive picture under the variations of Pr . In the following discussion we examine the scaling as well as the relative strengths of velocity structure functions for Pr ranging from 0.02 to 100. We compute the second, third, fifth, and seventh-order velocity structure functions using our numerical data (see Eq. (15)). We plot the second-order velocity structure function $S_2^u(l)$ versus l in Fig. 5(a), and the negative of third, fifth, and seventh-order velocity structure functions $[-S_3^u(l), -S_5^u(l), -S_7^u(l)]$ versus l in Fig. 5(b,c,d). We also plot the respective best-fit curves in the same figures. We observe that for $\text{Pr} \lesssim 1$, the third-order structure function exhibits Kolmogorov's scaling of $S_3^u(l) \sim -l$ over a range of intermediate scales that corresponds to the inertial range over which $E_u(k) \sim k^{-5/3}$ (as reported in Sec. IV A). In addition, for the above Prandtl numbers, the structure functions of orders $q = 2, 5, \text{ and } 7$ follow the predictions of She and Leveque [40] [see Figs. 5(a,c,d) and 6], as in hydrodynamic turbulence. The errors in the exponents range from ± 0.01 for the third-order structure functions to ± 0.05 for the seventh-order structure functions. Our

results are thus consistent with those of Sun *et al.* [46] and Bhattacharya *et al.* [50], but contrary to the studies that report Bolgiano-Obukhov scaling of the structure functions [41–44, 47].

Figure 5(a,b,c,d) also shows that the amplitudes of the velocity structure functions for all orders increase with decreasing Pr, similar to the amplitudes of the kinetic energy spectrum and flux. This is expected because the structure functions are directly related to the kinetic energy spectrum and flux [3, 4, 39], which show similar scaling (see Sec. IV).

The structure functions for Pr = 6.8 and 100 neither follow Kolmogorov’s scaling nor She-Leveque’s scaling; instead, they vary steeply at intermediate scales compared to those for Pr ≤ 1 (see Fig. 5). For Pr = 6.8, the structure functions scale as $S_2^u(l) \sim l^{1.87 \pm 0.02}$, $S_3^u(l) \sim -l^{2.87 \pm 0.02}$, $S_5^u(l) \sim -l^{4.45 \pm 0.04}$, and $S_7^u(l) \sim -l^{5.21 \pm 0.06}$. For Pr = 100, the curves are even steeper, with the structure functions scaling as $S_2^u(l) \sim l^{1.91 \pm 0.01}$, $S_3^u(l) \sim -l^{3.17 \pm 0.03}$, $S_5^u(l) \sim -l^{6.34 \pm 0.08}$, and $S_7^u(l) \sim -l^{8.2 \pm 0.2}$. Recall that in the limit of infinite Pr, the energy spectrum scales as $E_u(k) \sim k^{-13/3}$ due to strong viscous dissipation in the intermediate scales. A simple extrapolation of the above to the second, third, fifth, and seventh-order structure functions lead to $S_2^u(l) \sim l^{10/3}$, $S_3^u(l) \sim -l^5$, $S_5^u(l) \sim -l^{25/3}$, and $S_7^u(l) \sim -l^{35/3}$ respectively (without

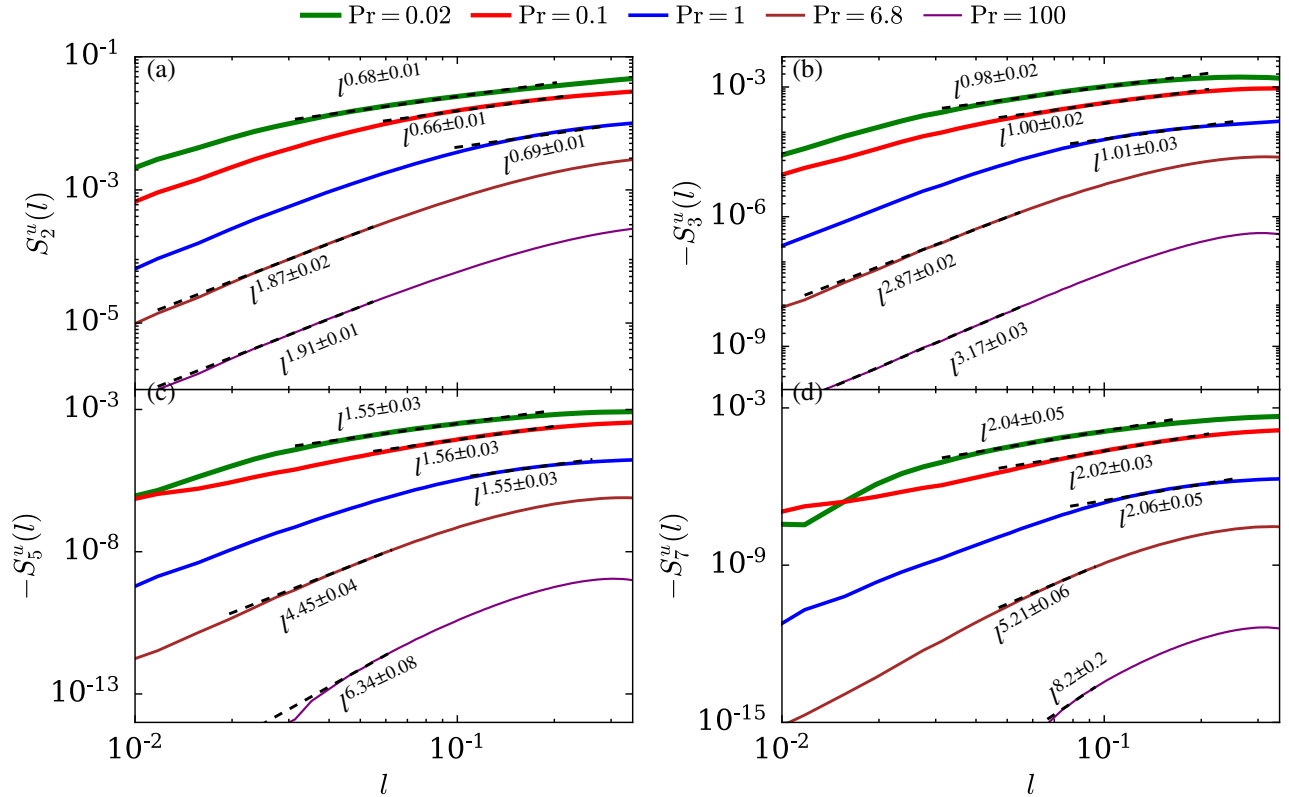


FIG. 5. (color online) For Pr = 0.02, 0.1, 1, 6.8, and 100: longitudinal velocity structure functions of orders (a) 2, (b) 3, (c) 5, and (d) 7 vs. l . The amplitudes of the structure functions decrease with the increase of Pr.

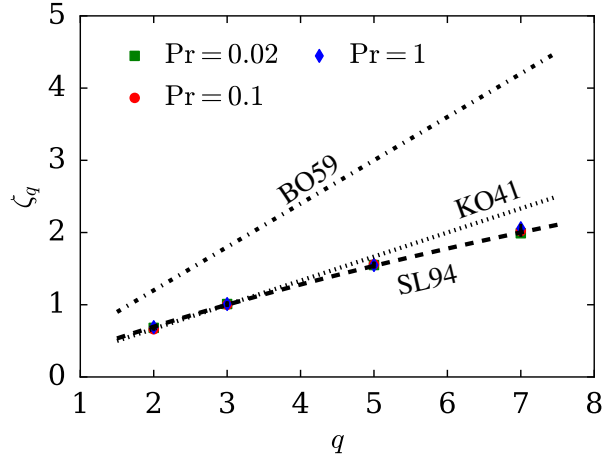


FIG. 6. (color online) For $\text{Pr} = 0.02, 0.1,$ and 1 : The scaling exponents ζ_q for the velocity structure functions vs. order q . The exponents match closely with the predictions of [40] (SL94). The figure also exhibits the extrapolated ζ_q 's for K41 ($q/3$) and Bolgiano-Obukhov (BO59) ($3q/5$).

intermittency effects [3]). The slopes of the structure functions computed using our data for $\text{Pr} = 6.8$ and 100 are not as steep as above predictions; this is possibly because the Prandtl numbers for our runs are finite and there are possible intermittency effects. Nevertheless, it is evident that the slopes of the structure functions for larger Prandtl numbers are significantly steeper than those for smaller Prandtl numbers.

In the next section, we discuss the Prandtl number effects on the probability distribution functions of convective heat flux.

VI. PRANDTL NUMBER DEPENDENCE OF LOCAL HEAT FLUX

There is a net heat transport in thermal convection, which is quantified using a nondimensional number called Nusselt number (Nu):

$$\text{Nu} = 1 + \frac{\langle u_z T \rangle}{\kappa \Delta / d}, \quad (21)$$

where T is the temperature field, and u_z is the vertical velocity. The Nusselt number is always positive, but the local vertical heat flux, given by $u_z T$, exhibits strong fluctuations [33, 51–53]. It has been observed that $u_z T$ take both positive and negative values, but the positive $u_z T$ dominates the negative ones leading to a net vertical heat flux. The strength of the fluctuations further vary in different regions inside the RBC domain; the fluctuations are strongest near the sidewalls [51] and weakest near the horizontal walls [52]. In this section, we present the variations of the probability distribution function (PDF) of $u_z T$ with the Prandtl number. In addition, we also study the horizontal heat fluxes, $u_x T$ and $u_y T$, which are expected to be symmetric so as to yield a zero net flux along the horizontal directions.

TABLE II. For $\text{Pr} = 0.02$ to 100 and $\text{Ra} = 10^7$: Standard deviations (σ_x , σ_y , and σ_z) of the local heat fluxes $u_x T$, $u_y T$, and $u_z T$ respectively, and the number of snapshots over which the PDFs of the above quantities are averaged. The standard deviations increase with Pr .

Pr	σ_x	σ_y	σ_z	Snapshots
0.02	36 ± 1	62 ± 1	64 ± 1	81
0.1	62 ± 5	87 ± 8	99 ± 7	66
1	125 ± 11	125 ± 11	173 ± 7	101
6.8	139 ± 16	138 ± 14	231 ± 13	101
100	140 ± 18	124 ± 16	296 ± 21	101

We compute the PDFs of the heat fluxes over the entire domain using our simulation data. The PDFs are averaged over 31 to 101 timeframes depending on the Prandtl numbers (see Table II). We plot the PDFs of the horizontal heat fluxes $u_x T$ and $u_y T$, normalized by $\kappa\Delta/d$, in Fig. 7(a,b) respectively, and the vertical heat flux $u_z T$, normalized by $\kappa\Delta/d$, in Fig. 7(c). Note that $\kappa = (\text{RaPr})^{-1/2}$ from Eq. (7). For all Prandtl numbers, the horizontal and vertical heat fluxes peak at zero. However, the horizontal heat fluxes are symmetric about their peaks, but the vertical heat fluxes show clear asymmetry with long tails in the positive direction. The asymmetry in the vertical flux yields a net vertical heat transport, but the symmetric horizontal fluxes sum to zero, as expected. These results are consistent with earlier studies [33, 51–53]. Both horizontal and vertical heat fluxes exhibit strong fluctuations near their most probable value of zero, causing noise-like ripples near the peaks of their PDFs.

A careful observation of the PDFs of Fig. 7 show an interesting feature: the fluctuations

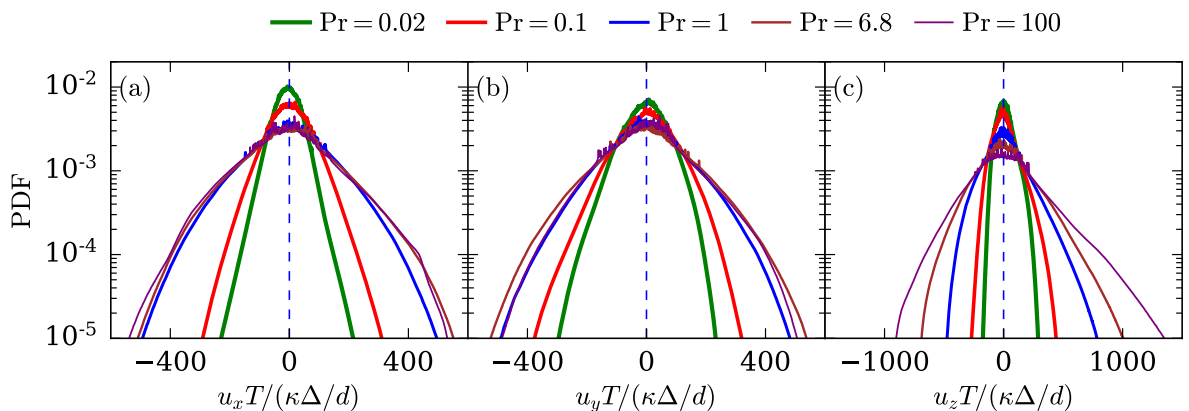


FIG. 7. (color online) For $\text{Ra} = 10^7$: The probability distribution functions (PDFs) of normalized local convective heat flux in the (a) x direction, (b) y direction, and (c) z direction for different Pr . The fluctuations of the local heat flux increase with Pr .

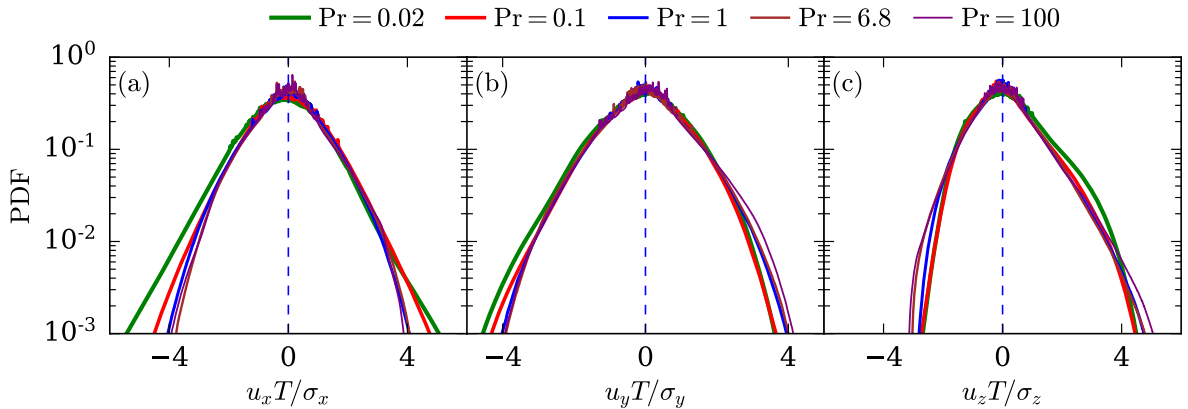


FIG. 8. (color online) For $Ra = 10^7$: The probability distribution functions (PDFs) of the local convective heat flux normalized with their respective standard deviations (σ_x , σ_y , σ_z) in the (a) x direction, (b) y direction, and (c) z direction. The normalized PDFs for different Prandtl numbers collapse into one curve.

in the local heat fluxes increase with the Prandtl numbers, which is evident from the long tails for $Pr \geq 1$. It is to be noted that for the same Rayleigh number, the thermal diffusivity, which is given by $\kappa = 1/\sqrt{RaPr}$, is strong for small Prandtl numbers. Hence, due to high thermal diffusivity, the heat transport is primarily via diffusion for small Pr , resulting in thick thermal plumes. The high value of thermal diffusivity and the thick plumes result in weak fluctuations of the local heat flux for small Pr . However, large- Pr convection takes place via thin thermal plumes due to weak thermal diffusivity, thereby inducing strong thermal fluctuations and inhomogeneity in the heat flux [36, 37, 60].

Interestingly, the PDFs of Fig. 7(a,b,c) can be collapsed into one curve each by normalizing the curves using the corresponding standard deviations. We present the collapsed curves in Fig. 8(a,b,c). The standard deviations are computed for every timeframe and then averaged. The computed standard deviations for different Prandtl numbers are tabulated in Table II. As expected, the standard deviations along with their respective errors increase with Prandtl number. There is, however, an anomaly in σ_y for $Pr = 100$ in that it is less than that for $Pr = 6.8$. However, we believe that this is a minor aberration that can be resolved by averaging over more timeframes.

We conclude in the next section.

VII. SUMMARY AND CONCLUSIONS

In this paper, using detailed numerical simulations of turbulent convection, we analyzed the Prandtl number dependence of the kinetic energy spectrum, flux, and the spectra of buoyant energy injection and viscous dissipation rates. Additionally, we examined the vari-

ations of velocity structure functions and the local heat flux with Pr . For our analysis, we varied Pr from 0.02 to 100, keeping the Rayleigh number fixed at $Ra = 10^7$.

Consistent with earlier works, the kinetic energy spectrum exhibits Kolmogorov scaling of $\sim k^{-5/3}$ for $Pr \leq 1$ and a steeper scaling of $\sim k^{-2.5}$ for $Pr \gg 1$ [10, 31, 32, 36, 37, 66, 89]. The inertial range is widest for $Pr = 0.02$, and it gets narrower as Pr is increased. The magnitudes of the kinetic energy spectrum and flux decrease with Pr , implying that flows with small Prandtl number have stronger nonlinear interactions among the velocity modes. The amplitudes of kinetic energy injection and dissipation rates follow a similar pattern as energy flux and spectrum. Our results are in agreement with earlier studies that report the Reynolds number to be a decreasing function of Pr [11, 58, 60, 62]. For $Pr \ll 1$, kinetic energy injection by buoyancy occurs mostly at large scales, causing the kinetic energy flux in the inertial range to be approximately equal to the viscous dissipation rate, similar to hydrodynamic turbulence. On the other hand, for $Pr \gg 1$, significant kinetic energy is injected at small scales as well, causing the energy flux to be a small fraction of the viscous dissipation rate.

The amplitudes of the velocity structure functions increase with the decrease of Pr , consistent with the results on energy spectrum. The velocity structure functions for $Pr \leq 1$ were shown to be in agreement with She-Leveque’s model, similar to hydrodynamic turbulence and consistent with earlier results [46, 50]. The structure functions exhibit steeper curves for $Pr = 6.8$ and 100 and are in agreement with the scaling of the energy spectrum for large Prandtl numbers.

The strength of fluctuations of the local convective heat flux increases with Pr . This is because the thick thermal plumes for small- Pr flows transfer heat efficiently throughout the flow, but thin thermal plumes for large- Pr flows create strong inhomogeneity in the heat flux.

Thus, our present study provides valuable insights into the variations of turbulent velocity and thermal fluctuations with Pr . Although we worked on a small set of parameters, we expect these patterns to be valid over a wide range of Ra and Pr , with the possible exception of the ultimate regime [38]. We expect these results to be important for modeling flows in stars, bubbly turbulence, and liquid metal batteries. Further, our analysis should also help in developing accurate subgrid models for convection.

ACKNOWLEDGEMENTS

The authors are grateful to Roshan Samuel and Syed Fahad Anwer for their important contributions in the development of the finite difference code SARAS. Further, the authors thank Shadab Alam and Soumyadeep Chatterjee for useful discussions. Our numerical simulations were performed on Shaheen II of KAUST supercomputing laboratory, Saudi Arabia (under the project k1416) and on HPC2013 of IIT Kanpur, India.

Appendix A: Entropy spectra and flux of RBC

In this section, we compute the nondimensionalized entropy spectra, $E_\theta(k)$, and entropy fluxes, $\Pi_\theta(k)$, of RBC using our data for different Pr, with $Ra = 10^7$. These quantities are computed as follows:

$$E_\theta(k) = \frac{1}{2} \sum_{k \leq |\mathbf{k}'| < k+1} |\theta(\mathbf{k}')|^2, \quad (\text{A1})$$

$$\Pi_\theta(k_0) = \sum_{k \geq k_0} \sum_{p < k_0} \delta_{\mathbf{k}, \mathbf{p}+\mathbf{q}} \Im([\mathbf{k} \cdot \mathbf{u}(\mathbf{q})][\theta^*(\mathbf{k})\theta(\mathbf{p})]). \quad (\text{A2})$$

We plot the entropy spectra and fluxes for $Pr = 1, 6.8,$ and 100 in Fig. 9(a,b), and for $Pr = 0.02$ and 0.1 in Fig. 10(a,b). The figures show that the nondimensional entropy are approximately the same for all Prandtl numbers, unlike the kinetic energy spectrum that decreases with the increase of Pr. The entropy flux, however, decreases with the increase of Pr because the entropy flux is proportional to the velocity fluctuations (see Eq. (A2)), which are strong for flows with small Pr.

The entropy spectrum exhibits dual branch for $Pr = 1, 6.8,$ and 100 , with the upper branch scaling as $\sim k^{-2.13 \pm 0.08}$. Mishra and Verma [31] and Pandey *et al.* [36] explained this branch in terms of the temperature modes $\theta(0, 0, 2n)$, which are approximately equal to $-1/(2n\pi)$ for thin thermal boundary layers (n being an integer). The lower branch, which is constituted by the remaining modes, does not exhibit any clear scaling. The temperature modes of both the branches yield the constant entropy flux (see Fig. 9(b)).

For $Pr = 0.02$ and 0.1 , the entropy spectrum again has two branches; however, the

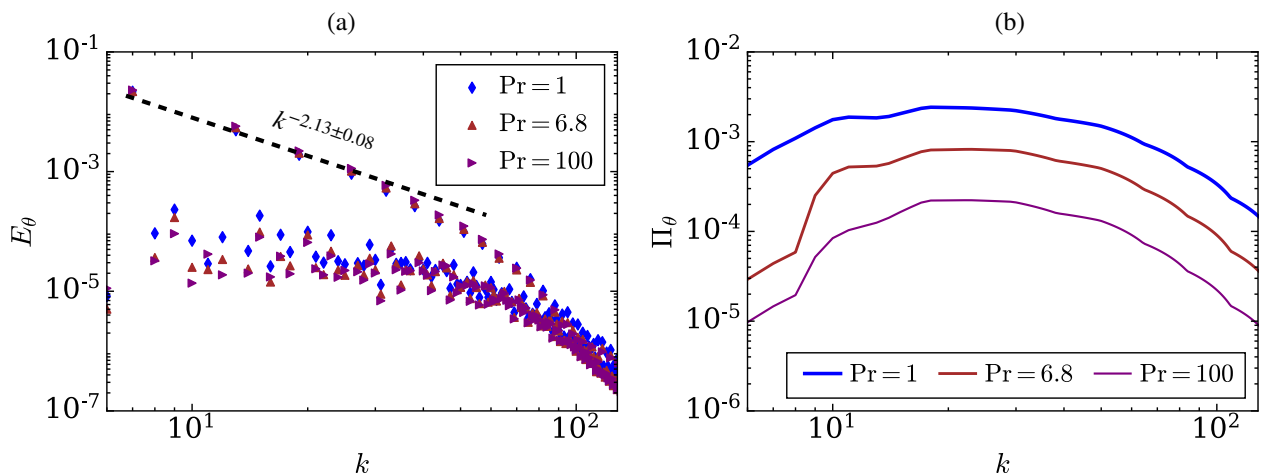


FIG. 9. (color online) For $Ra = 10^7$ and $Pr = 1, 6.8,$ and 100 : (a) Entropy spectrum E_θ (with dual branches) and (b) entropy flux Π_θ vs. k . The amplitudes of the entropy spectrum do not vary with Pr, but the amplitudes of the entropy flux decrease with increase of Pr.

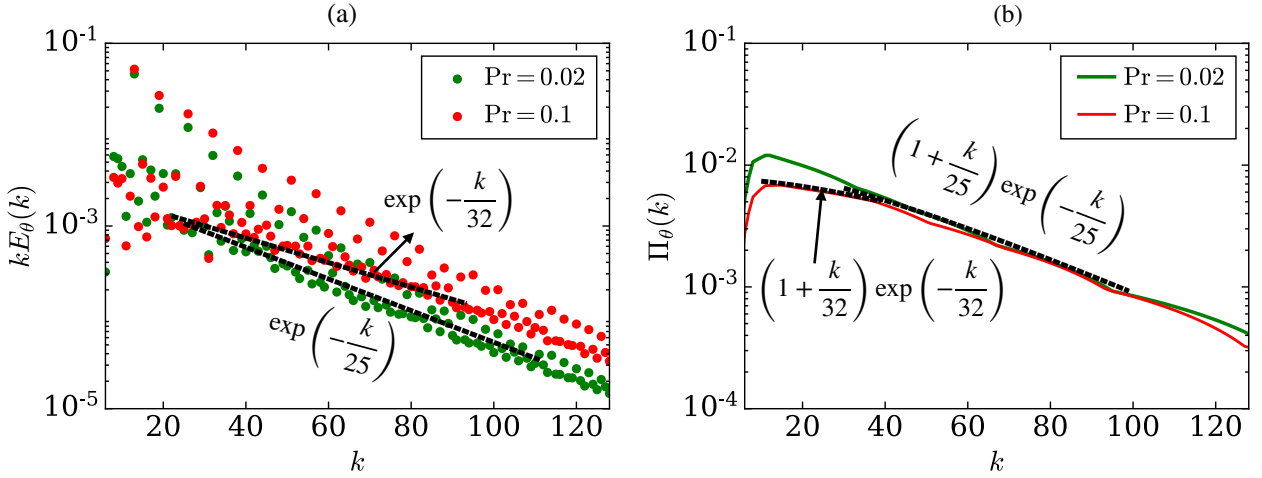


FIG. 10. (color online) For $Ra = 10^7$ and $Pr = 0.02$ and 0.1 : Semi-log plots of (a) normalized entropy spectrum kE_θ and (b) entropy flux Π_θ vs. k . The lower branch of the entropy spectrum and the entropy flux fit well with exponential function.

upper branch is not very prominent because of thick thermal boundary layers. For small- Pr convection, the nonlinear term of the θ -equation [Eq. (3)] is small compared to the diffusive term, similar to the momentum equation for laminar flows. Following the arguments of Martínez *et al.* [90] and Verma *et al.* [91] for energy spectrum of laminar flows, we propose that the entropy spectrum for small- Pr convection is of the following exponential form:

$$E_\theta(k) \sim k^{-1}(k/k_c) \exp(-k/k_c), \quad (\text{A3})$$

where k_c is the wavenumber beyond which the thermal energy dissipation becomes dominant.

Now, for a steady state, the entropy flux is related to entropy injection (\mathcal{F}_θ) and dissipation spectra ($2\kappa k^2 E_\theta$) by the variable entropy flux equation:

$$\frac{d\Pi_\theta}{dk} = \mathcal{F}_\theta(k) - 2\kappa k^2 E_\theta(k), \quad (\text{A4})$$

In the intermediate wavenumbers for small- Pr convection, the spectrum of entropy dissipation dominates that of the entropy injection rate; hence $2\kappa k^2 E_\theta(k) \gg \mathcal{F}_\theta(k)$. Using this condition and substituting the expression of Eq. (A3) in Eq. (A4), we obtain the following:

$$\frac{d\Pi_\theta}{dk} \sim k \exp(-k/k_c). \quad (\text{A5})$$

Integration of the above expression yields the following expression for the entropy flux:

$$\Pi_\theta(k) \sim (1 + k/k_c) \exp(-k/k_c). \quad (\text{A6})$$

Our above arguments closely resemble the derivation of the energy flux for small- Re flows [91], and for quasi-static magnetohydrodynamic turbulence with strong interaction parameters [92].

Figure 10(a) shows that the lower branch of the entropy spectrum fits well with Eq. (A3) in the intermediate wavenumbers, with $k_c = 32$ for $\text{Pr} = 0.1$ and $k_c = 25$ for $\text{Pr} = 0.02$. Further, as evident from Fig. 10(b), the entropy fluxes for $\text{Pr} = 0.1$ and 0.02 obey Eq. (A6). Our results are consistent with earlier studies [14, 15, 31] that also obtained similar exponential scalings in the entropy spectrum and flux of small-Pr convection.

-
- [1] A. N. Kolmogorov, Dissipation of Energy in Locally Isotropic Turbulence, Dokl Acad Nauk SSSR **32**, 16 (1941).
 - [2] A. N. Kolmogorov, The local structure of turbulence in incompressible viscous fluid for very large Reynolds numbers, Dokl Acad Nauk SSSR **30**, 301 (1941).
 - [3] U. Frisch, *Turbulence: The Legacy of A. N. Kolmogorov* (Cambridge University Press, Cambridge, 1995).
 - [4] M. Lesieur, *Turbulence in Fluids* (Springer-Verlag, Dordrecht, 2008).
 - [5] R. Bolgiano, Turbulent spectra in a stably stratified atmosphere, J. Geophys. Res. **64**, 2226 (1959).
 - [6] A. M. Obukhov, On influence of buoyancy forces on the structure of temperature field in a turbulent flow, Dokl Acad Nauk SSSR **125**, 1246 (1959).
 - [7] I. Procaccia and R. Zeitak, Scaling exponents in nonisotropic convective turbulence, Phys. Rev. Lett. **62**, 2128 (1989).
 - [8] V. S. L'vov, Spectra of velocity and temperature-fluctuations with constant entropy flux of fully-developed free-convective turbulence, Phys. Rev. Lett. **67**, 687 (1991).
 - [9] V. S. L'vov and G. Falkovich, Conservation laws and two-flux spectra of hydrodynamic convective turbulence, Physica D **57**, 85 (1992).
 - [10] A. Kumar, A. G. Chatterjee, and M. K. Verma, Energy spectrum of buoyancy-driven turbulence, Phys. Rev. E **90**, 023016 (2014).
 - [11] G. Ahlers, S. Grossmann, and D. Lohse, Heat transfer and large scale dynamics in turbulent Rayleigh-Bénard convection, Rev. Mod. Phys. **81**, 503 (2009).
 - [12] D. Lohse and K.-Q. Xia, Small-scale properties of turbulent Rayleigh-Bénard convection, Annu. Rev. Fluid Mech. **42**, 335 (2010).
 - [13] F. Chillà and J. Schumacher, New perspectives in turbulent Rayleigh-Bénard convection, Eur. Phys. J. E **35**, 58 (2012).
 - [14] M. K. Verma, *Physics of Buoyant Flows: From Instabilities to Turbulence* (World Scientific, Singapore, 2018).
 - [15] M. K. Verma, *Energy transfers in Fluid Flows: Multiscale and Spectral Perspectives* (Cambridge University Press, Cambridge, 2019).
 - [16] S. Chandrasekhar, *Hydrodynamic and Hydromagnetic Stability* (Dover publications, Oxford, 1981).

- [17] R. Rubinstein, *Renormalization group theory of Bolgiano scaling in Boussinesq turbulence*, Tech. Rep. ICOM-94-8; CMOTT-94-2 (1994).
- [18] R. M. Kerr, Rayleigh number scaling in numerical convection, *J. Fluid Mech.* **310**, 139 (1996).
- [19] S. Ashkenazi and V. Steinberg, Spectra and statistics of velocity and temperature fluctuations in turbulent convection, *Phys. Rev. Lett.* **83**, 4760 (1999).
- [20] X.-D. Shang and K.-Q. Xia, Scaling of the velocity power spectra in turbulent thermal convection, *Phys. Rev. E* **64**, 065301(R) (2001).
- [21] X.-Z. Wu, L. P. Kadanoff, A. Libchaber, and M. Sano, Frequency power spectrum of temperature fluctuations in free convection, *Phys. Rev. Lett.* **64**, 2140 (1990).
- [22] J. J. Niemela, L. Skrbek, K. R. Sreenivasan, and R. J. Donnelly, Turbulent convection at very high Rayleigh numbers, *Nature* **404**, 837 (2000).
- [23] F. Chillà, S. Ciliberto, C. Innocenti, and E. Pampaloni, Spectra of Local and Averaged Scalar Fields in Turbulence, *EPL* **22**, 23 (1993).
- [24] S.-Q. Zhou and K.-Q. Xia, Scaling properties of the temperature field in convective turbulence, *Phys. Rev. Lett.* **87**, 064501 (2001).
- [25] S. Cioni, S. Ciliberto, and J. Sommeria, Temperature structure functions in turbulent convection at low prandtl number, *EPL* **32**, 413 (1995).
- [26] T. Takeshita, T. Segawa, J. A. Glazier, and M. Sano, Thermal turbulence in mercury, *Phys. Rev. Lett.* **76**, 1465 (1996).
- [27] R. Camussi and R. Verzicco, Convective turbulence in mercury: scaling laws and spectra, *Phys. Fluids* **10**, 516 (1998).
- [28] S. Horanyi, L. Krebs, and U. Müller, Turbulent rayleigh–bénard convection in low prandtl–number fluids, *Int. J. Heat Mass Transf.* **42**, 3983 (1999).
- [29] P. Frick, R. Khalilov, I. Kolesnichenko, A. Mamykin, V. Pakholkov, A. Pavlinov, and S. Rogozhkin, Turbulent convective heat transfer in a long cylinder with liquid sodium, *EPL* **109**, 14002 (2015).
- [30] J. Schumacher, P. Götzfried, and J. D. Scheel, Enhanced enstrophy generation for turbulent convection in low-Prandtl-number fluids., *PNAS* **112**, 201505111 (2015).
- [31] P. K. Mishra and M. K. Verma, Energy spectra and fluxes for Rayleigh–Bénard convection, *Phys. Rev. E* **81**, 056316 (2010).
- [32] M. K. Verma, A. Kumar, and A. Pandey, Phenomenology of buoyancy-driven turbulence: recent results, *New J. Phys.* **19**, 025012 (2017).
- [33] M. Kaczorowski and K.-Q. Xia, Turbulent flow in the bulk of Rayleigh–Bénard convection: small-scale properties in a cubic cell, *J. Fluid Mech.* **722**, 596 (2013).
- [34] R. P. J. Kunnen and H. J. H. Clercx, Probing the energy cascade of convective turbulence, *Phys. Rev. E* **90**, 063018 (2014).
- [35] J. K. Bhattacharjee, Kolmogorov argument for the scaling of the energy spectrum in a stratified fluid, *Phys. Lett. A* **379**, 696 (2015).

- [36] A. Pandey, M. K. Verma, and P. K. Mishra, Scaling of heat flux and energy spectrum for very large Prandtl number convection, *Phys. Rev. E* **89**, 023006 (2014).
- [37] A. Pandey, M. K. Verma, A. G. Chatterjee, and B. Dutta, Similarities between 2D and 3D convection for large Prandtl number, *Pramana-J. Phys.* **87**, 13 (2016).
- [38] R. H. Kraichnan, Turbulent thermal convection at arbitrary prandtl number, *Phys. Fluids* **5**, 1374 (1962).
- [39] E. S. C. Ching, *Statistics and Scaling in Turbulent Rayleigh-Bénard Convection* (Springer, Berlin, 2013).
- [40] Z.-S. She and E. Leveque, Universal scaling laws in fully developed turbulence, *Phys. Rev. Lett.* **72**, 336 (1994).
- [41] R. Benzi, F. Massaioli, S. Succi, and R. Tripiccione, Scaling behaviour of the velocity and temperature correlation functions in 3D convective turbulence, *EPL* **28**, 231 (1994).
- [42] R. Benzi, R. Tripiccione, F. Massaioli, S. Succi, and S. Ciliberto, On the scaling of the velocity and temperature structure functions in Rayleigh-Bénard convection, *EPL* **25**, 341 (1994).
- [43] E. S. C. Ching, Intermittency of temperature field in turbulent convection, *Phys. Rev. E* **61**, R33 (2000).
- [44] E. Calzavarini, F. Toschi, and R. Tripiccione, Evidences of Bolgiano-Obhukhov scaling in three-dimensional Rayleigh-Bénard convection, *Phys. Rev. E* **66**, 016304 (2002).
- [45] E. S. C. Ching and W. C. Cheng, Anomalous scaling and refined similarity of an active scalar in a shell model of homogeneous turbulent convection, *Phys. Rev. E* **77**, 015303(R) (2008).
- [46] C. Sun, Q. Zhou, and K.-Q. Xia, Cascades of velocity and temperature fluctuations in buoyancy-driven thermal turbulence, *Phys. Rev. Lett.* **97**, 144504 (2006).
- [47] R. P. J. Kunnen, H. J. H. Clercx, B. J. Geurts, L. J. A. van Bokhoven, R. A. D. Akkermans, and R. Verzicco, Numerical and experimental investigation of structure-function scaling in turbulent Rayleigh-Bénard convection, *Phys. Rev. E* **77**, 016302 (2008).
- [48] E. S. C. Ching, Y.-K. Tsang, T. N. Fok, X. He, and P. Tong, Scaling behavior in turbulent Rayleigh-Bénard convection revealed by conditional structure functions, *Phys. Rev. E* **87**, 013005 (2013).
- [49] E. S. C. Ching, Scaling laws in the central region of confined turbulent thermal convection, *Phys. Rev. E* **75**, 056302 (2007).
- [50] S. Bhattacharya, S. Sadhukhan, A. Guha, and M. K. Verma, Similarities between the structure functions of thermal convection and hydrodynamic turbulence, *Phys. Fluids* **31**, 115107 (2019).
- [51] X.-D. Shang, X.-L. Qiu, P. Tong, and K.-Q. Xia, Measured local heat transport in turbulent Rayleigh-Bénard convection, *Phys. Rev. Lett.* **90**, 074501 (2003).
- [52] O. Shishkina and C. Wagner, Local heat fluxes in turbulent Rayleigh-Bénard convection, *Phys. Fluids* **19**, 085107 (2007).
- [53] H. K. Pharasi, D. Kumar, K. Kumar, and J. K. Bhattacharjee, Spectra and probability distributions of thermal flux in turbulent Rayleigh-Bénard convection, *Phys. Fluids* **28**, 055103

- (2016).
- [54] E. Falcon, S. Aumaitre, C. Falcon, C. Laroche, and S. Fauve, Fluctuations of energy flux in wave turbulence, *Phys. Rev. Lett.* **100**, 064503 (2008).
 - [55] S. Grossmann and D. Lohse, Thermal convection for large Prandtl numbers, *Phys. Rev. Lett.* **86**, 3316 (2001).
 - [56] S. Grossmann and D. Lohse, Scaling in thermal convection: a unifying theory, *J. Fluid Mech.* **407**, 27 (2000).
 - [57] A. Pandey and M. K. Verma, Scaling of large-scale quantities in Rayleigh-Bénard convection, *Phys. Fluids* **28**, 095105 (2016).
 - [58] R. Verzicco and R. Camussi, Prandtl number effects in convective turbulence, *J. Fluid Mech.* **383**, 55 (1999).
 - [59] G. Ahlers and X. Xu, Prandtl-number dependence of heat transport in turbulent Rayleigh-Bénard convection, *Phys. Rev. Lett.* **86**, 3320 (2001).
 - [60] G. Silano, K. R. Sreenivasan, and R. Verzicco, Numerical simulations of Rayleigh-Bénard convection for Prandtl numbers between 10^{-1} and 10^4 and Rayleigh numbers between 10^5 and 10^9 , *J. Fluid Mech.* **662**, 409 (2010).
 - [61] K.-Q. Xia, S. Lam, and S.-Q. Zhou, Heat-flux measurement in high-Prandtl-number turbulent Rayleigh-Bénard convection, *Phys. Rev. Lett.* **88**, 064501 (2002).
 - [62] S. Lam, X.-D. Shang, S.-Q. Zhou, and K.-Q. Xia, Prandtl number dependence of the viscous boundary layer and the Reynolds numbers in Rayleigh-Bénard convection, *Phys. Rev. E* **65**, 066306 (2002).
 - [63] B. I. Shraiman and E. D. Siggia, Heat transport in high-Rayleigh-number convection, *Phys. Rev. A* **42**, 3650 (1990).
 - [64] O. Shishkina, M. S. Emran, S. Grossmann, and D. Lohse, Scaling relations in large-Prandtl-number natural thermal convection, *Phys. Rev. Fluids* **2**, 103502 (2017).
 - [65] M. S. Emran and J. Schumacher, Fine-scale statistics of temperature and its derivatives in convective turbulence, *J. Fluid Mech.* **611**, 13 (2008).
 - [66] A. Kumar and M. K. Verma, Shell model for buoyancy-driven turbulence., *Phys. Rev. E* **91**, 043014 (2015).
 - [67] R. H. Kraichnan, The structure of isotropic turbulence at very high Reynolds numbers, *J. Fluid Mech.* **5**, 497 (1959).
 - [68] G. Dar, M. K. Verma, and V. Eswaran, Energy transfer in two-dimensional magnetohydrodynamic turbulence: formalism and numerical results, *Physica D* **157**, 207 (2001).
 - [69] M. K. Verma, Statistical theory of magnetohydrodynamic turbulence: recent results, *Phys. Rep.* **401**, 229 (2004).
 - [70] L. D. Landau and E. M. Lifshitz, *Fluid Mechanics*, 2nd ed., Course of Theoretical Physics (Elsevier, Oxford, 1987).
 - [71] M. K. Verma, R. J. Samuel, S. Chatterjee, S. Bhattacharya, and A. Asad, Challenges in fluid

- flow simulations using exascale computing, *S.N. Comput. Sci.* **1**, 178 (2020).
- [72] R. J. Samuel, S. Bhattacharya, A. Asad, S. Chatterjee, M. K. Verma, R. Samtaney, and S. F. Anwer, SARAS: A general-purpose PDE solver for fluid dynamics, *J. Open Source Softw.* (unpublished) (2020).
- [73] G. Grötzbach, Spatial resolution requirements for direct numerical simulation of the Rayleigh-Bénard convection, *J. Comput. Phys* **49**, 241 (1983).
- [74] R. Verzicco and R. Camussi, Numerical experiments on strongly turbulent thermal convection in a slender cylindrical cell, *J. Fluid Mech.* **477**, 19 (2003).
- [75] A. Pandey, A. Kumar, A. G. Chatterjee, and M. K. Verma, Dynamics of large-scale quantities in Rayleigh-Bénard convection, *Phys. Rev. E* **94**, 053106 (2016).
- [76] S. Bhattacharya, A. Pandey, A. Kumar, and M. K. Verma, Complexity of viscous dissipation in turbulent thermal convection, *Phys. Fluids* **30**, 031702 (2018).
- [77] S. Bhattacharya, R. Samtaney, and M. K. Verma, Scaling and spatial intermittency of thermal dissipation in turbulent convection, *Phys. Fluids* , 1 (2019).
- [78] J. D. Scheel and J. Schumacher, Predicting transition ranges to fully turbulent viscous boundary layers in low Prandtl number convection flows, *Phys. Rev. Fluids* **2**, 123501 (2017).
- [79] R. Vishnu and A. Sameen, Heat transfer scaling in natural convection with shear due to rotation, *Phys. Rev. Fluids* **5**, 113504 (2020).
- [80] A. G. Chatterjee, M. K. Verma, A. Kumar, R. Samtaney, B. Hadri, and R. Khurram, Scaling of a Fast Fourier Transform and a pseudo-spectral fluid solver up to 196608 cores, *J. Parallel Distrib. Comput.* **113**, 77 (2018).
- [81] M. K. Verma, A. G. Chatterjee, R. K. Yadav, S. Paul, M. Chandra, and R. Samtaney, Benchmarking and scaling studies of pseudospectral code Tarang for turbulence simulations, *Pramana-J. Phys.* **81**, 617 (2013).
- [82] S. Bhattacharya, M. K. Verma, and R. Samtaney, Revisiting Reynolds and Nusselt numbers in turbulent thermal convection, *Phys. Fluids* **33**, 015113 (2021).
- [83] D. Nath, A. Pandey, A. Kumar, and M. K. Verma, Near isotropic behavior of turbulent thermal convection, *Phys. Rev. Fluids* **1**, 064302 (2016).
- [84] S. Sadhukhan, S. Bhattacharya, and M. K. Verma, fastSF: A parallel code for computing the structure functions of turbulence, *J. Open Source Softw.* **6**, 2185 (2021).
- [85] R. Stepanov, F. Plunian, M. Kessar, and G. Balarac, Systematic bias in the calculation of spectral density from a three-dimensional spatial grid, *Phys. Rev. E* **90**, 053309 (2014).
- [86] M. K. Verma, Contrasting turbulence in stably stratified flows and thermal convection, *Phys. Scr.* **94**, 1 (2019).
- [87] K. R. Sreenivasan and R. A. Antonia, The phenomenology of small-scale turbulence, *Annu. Rev. Fluid Mech.* **29**, 435 (1997).
- [88] M. K. Verma, Introduction to Statistical Theory of Fluid Turbulence, arXiv (2005).
- [89] A. Kumar and M. K. Verma, Applicability of Taylor’s hypothesis in thermally driven turbu-

- lence, R. Soc. open sci. **5**, 172152 (2018).
- [90] D. O. Martínez, S. Chen, G. D. Doolen, R. H. Kraichnan, L.-P. Wang, and Y. Zhou, Energy spectrum in the dissipation range of fluid turbulence, J. Plasma Phys. **57**, 195 (1997).
- [91] M. K. Verma, A. Kumar, P. Kumar, S. Barman, A. G. Chatterjee, R. Samtaney, and R. Stepanov, Energy Spectra and Fluxes in Dissipation Range of Turbulent and Laminar Flows, Fluid Dyn. **53**, 728 (2018).
- [92] M. K. Verma and K. S. Reddy, Modeling quasi-static magnetohydrodynamic turbulence with variable energy flux, Phys. Fluids **27**, 025114 (2015).